

Hadley Cell Widening: Model Simulations versus Observations

CELESTE M. JOHANSON AND QIANG FU

Department of Atmospheric Sciences, University of Washington, Seattle, Washington

(Manuscript received 8 May 2008, in final form 10 September 2008)

ABSTRACT

Observations show that the Hadley cell has widened by about 2° – 5° since 1979. This widening and the concomitant poleward displacement of the subtropical dry zones may be accompanied by large-scale drying near 30°N and 30°S . Such drying poses a risk to inhabitants of these regions who are accustomed to established rainfall patterns. Simple and comprehensive general circulation models (GCMs) indicate that the Hadley cell may widen in response to global warming, warming of the west Pacific, or polar stratospheric cooling. The combination of these factors may be responsible for the recent observations. But there is no study so far that has compared the observed widening to GCM simulations of twentieth-century climate integrated with historical changes in forcings. Here the Hadley cell widening is assessed in current GCMs from historical simulations of the twentieth century as well as future climate projections and preindustrial control runs. The authors find that observed widening cannot be explained by natural variability. This observed widening is also significantly larger than in simulations of the twentieth and twenty-first centuries. These results illustrate the need for further investigation into the discrepancy between the observed and simulated widening of the Hadley cell.

1. Introduction

The Hadley cell is a large-scale atmospheric circulation driven by differential heating of the earth's surface: warm, moist air rises near the equator, diverges poleward in the upper troposphere, and subsides in the subtropics (e.g., Wallace and Hobbs 2006). The subsiding air is both warm and dry, having lost moisture through precipitation while retaining latent energy from condensation occurring in the upward branch. Because this large-scale sinking suppresses convection, the subtropical dry zone located below the subsiding branch of the Hadley cell is dry, warm, and cloud free. The boundaries of the Hadley cell, which also mark the boundaries of the tropics, are characterized by the poleward extent of subsidence in the subtropical dry zones and by the locations of the subtropical jets (e.g., Seidel et al. 2008).

New evidence indicates that the subtropical jets have been shifting poleward since 1979. Changes in meridional temperature gradients in the vicinity of the jets are associated with their poleward displacements in accordance with the thermal wind balance. Such changes, obtained from satellite observations of tropospheric

temperature trends, suggest a total Hadley cell widening of $\sim 2^{\circ}$ of latitude since 1979 (Fu et al. 2006). The subtropical jet also marks the boundary between regions of relatively small total column ozone in the tropics with higher values in the midlatitudes (Hudson et al. 2003). Satellite observations of total column ozone in the Northern Hemisphere reveal an increase in the relative area of the tropical ozone regime, implying a poleward displacement of the Northern Hemisphere jet by $\sim 2.7^{\circ}$ (Hudson et al. 2006). Other empirical evidence of Hadley cell widening over both hemispheres is given by a poleward shift of outgoing longwave radiation (OLR) contours at the boundaries of the tropics (Hu and Fu 2007), increased frequency of higher subtropical tropopause heights (Seidel and Randel 2007), and the poleward displacement of subsidence in the subtropical dry zones (Hu and Fu 2007). Collectively, observational evidence indicates that the Hadley cell has widened by $\sim 2^{\circ}$ – 5° since 1979 (Seidel et al. 2008).

The widening of the subtropical dry zones may lead to desertification poleward of their current climatological boundaries with potentially serious consequences for inhabitants accustomed to established precipitation patterns. Because the underlying causes of the recent widening are still unknown (Seidel et al. 2008), it is crucial that global climate (general circulation) models (GCMs) properly simulate the observed widening so as to isolate

Corresponding author address: Celeste Johanson, University of Washington, Box 351640, Seattle, WA 98195.
E-mail: celestej@atmos.washington.edu

the relevant forcings and their relative contributions. So far, attempts to understand recent changes in Hadley cell width have focused on comparing observations to GCM simulations of twenty-first-century climate (Lu et al. 2007) and idealized GCMs (Frierson et al. 2007). Other studies of poleward shifts in zonal mean circulations related to the Hadley cell have focused solely on projected changes during the twenty-first century (Yin 2005; Previdi and Liepert 2007). Although all of these studies suggest a widening of the Hadley cell over the twenty-first century associated with global warming, the model projected rate is much smaller than the observations (e.g., Lu et al. 2007).

There are fundamental differences in external forcings between twenty-first- and twentieth-century climates. Greenhouse gases will continue to increase during this century owing to human activities (Solomon et al. 2007), but stratospheric ozone will begin to recover as ozone depleting substances are phased out (e.g., Eyring et al. 2007). Strong polar stratospheric cooling associated with ozone depletion since 1979 has significantly altered circulations in the stratosphere and troposphere (e.g., Thompson and Solomon 2002). Idealized GCMs find that polar stratospheric cooling leads to Hadley cell widening (Polvani and Kushner 2002), which suggests that ozone depletion may be at least partially responsible for the recent widening. If this is true, ozone recovery during the twenty-first century would partially compensate the tropical widening associated with global warming. However, since 1979 ozone depletion and increases of greenhouse gases may have forced the climate system in the same direction.

Until now, no study has compared the recent widening to twentieth-century climate model simulations integrated with historical changes in external forcings. One of the primary goals of this work is to provide such a comparison. In addition, we ask whether the observations of Hadley cell widening can be explained by internal climate variability. Finally, we compare projections of widening in the future to recent observations and to simulations of twentieth-century climate. Observations of Hadley cell width and GCM simulations are described in section 2. Comparisons among observations and model simulations are given in section 3. Plausible mechanisms for the observed widening are discussed in section 4, and conclusions are given in section 5.

2. Data and methods

a. Measures of Hadley cell width

We determine the Hadley cell width with three different measures following Lu et al. (2007) and Hu and Fu

(2007). The first way of defining the Hadley cell edges is to find the latitudes where meridional mass flux in the troposphere becomes zero poleward of the subtropical maxima. Meridional mass flux at 500 hPa is defined by

$$\psi_{500} = \frac{2\pi a \cos \varphi}{g} \int_0^{500} [v] dp, \quad (1)$$

where $[v]$ is the zonal mean meridional wind, a is the earth's radius, φ is latitude, and g is gravity. The total width of the Hadley cell is thus given by the distance between the latitudes in each hemisphere where $\psi_{500} = 0 \text{ kg s}^{-1}$.

The edges of the Hadley cell may also be identified by the zonal mean OLR contours in the subtropics (Hu and Fu 2007). The largest values of OLR are found in the subtropics as a result of the lack of high clouds and general aridity in these regions. OLR decreases rapidly from the subtropics to the midlatitudes with typical values in the transition zone near 250 W m^{-2} . Hadley cell width is thus given by the distance between latitudes where $\text{OLR} = 250 \text{ W m}^{-2}$ in each hemisphere's subtropical transition zone.

A third method of inferring the Hadley cell width involves the zonal mean distribution of precipitation minus evaporation ($P - E$) (e.g., Lu et al. 2007). Zonal mean $P - E$ is largest in the rising branch of the Hadley cell near the equator. It is negative in the subtropics where subsidence dominates and then becomes positive again in the midlatitudes. The Hadley cell edges are identified by the latitudes where $P - E$ becomes zero on the poleward sides of the subtropical minima. In this study, we first determine the edges of the Hadley cell for each season and then derive annual-mean Hadley cell edge positions by averaging together the seasonal values. All variables are then analyzed in terms of annual-mean and zonal averages.

b. Observational and model data

Time series of Hadley cell widths from satellite-observed OLR and reanalysis-derived ψ_{500} were obtained following Hu and Fu (2007). The three OLR records were from the High Resolution Infrared Radiation Sounder (HIRS) pathfinder dataset (Mehta and Susskind 1999), the International Satellite Cloud Climatology Project (ISCCP) version FD dataset (Zhang et al. 2004), and the Global Energy and Water Cycle Experiment (GEWEX) Radiative Flux Assessment (RFA) dataset (Stackhouse et al. 2004). The time periods used here are from December 1979 to November 2002 for HIRS, and from December 1983 to November 2004 for the ISCCP and GEWEX datasets.

The three reanalyses were from the 40-yr European Centre for Medium-Range Weather Forecasts Re-Analysis (ERA-40) (Uppala et al. 2005), the National Centers for Environmental Prediction–National Center for Atmospheric Research (NCEP–NCAR) (Kistler et al. 2001), and the National Centers for Environmental Prediction–Department of Energy (NCEP–DOE) (Kanamitsu et al. 2002). The ERA-40 used here is from January 1979 to December 2001, and the NCEP–NCAR and NCEP–DOE reanalyses are from January 1979 to December 2005. Although reanalysis data are available for years prior to 1979, their reliability increased after 1979 as satellite data became available. In these datasets, ψ_{500} is given by the average streamfunction between 400 and 600 hPa. The results are not sensitive to calculating ψ_{500} from this averaging instead of finding ψ_{500} directly following Eq. (1).

We use model results from preindustrial control runs and simulations of the twentieth and twenty-first centuries from a collection of 25 GCMs. The model results are from the World Climate Research Programme (WCRP) Coupled Model Intercomparison Project phase 3 (CMIP3) multimodel dataset (Meehl et al. 2007), which are those used in Solomon et al. (2007). Additional atmosphere-only simulations from 14 GCMs using prescribed sea surface temperatures based on observations were obtained from the Atmospheric Model Intercomparison Project phase 2 (AMIP2). AMIP2 is a continuation of the original Atmospheric Model Intercomparison Project (AMIP) (Gates et al. 1999) but with a longer integration period and improved boundary conditions. (The current state of the AMIP2 project is described online at <http://www-pcmdi.llnl.gov/projects/amip/index.php>.) Model data from AMIP2 and the historical simulations of CMIP3 are obtained starting in 1979 to facilitate comparison with the observations. The models have horizontal resolution ranging from $\sim 1.1^\circ$ to 4° of latitude, between 12 and 56 vertical levels, and model tops from 25 to 0.05 hPa. Details of the models and experiments are given in Tables 1 and 2, and in the appendix (Tables A1 and A2).

Projections of twenty-first-century climate are from the CMIP3 simulations integrated with different Special Report on Emission Scenarios (SRES) (Nakicenovic and Swart 2000) scenarios. We focus on model results with scenarios A2, A1B, and B1, corresponding to high, medium, and low radiative forcings, respectively. The CO_2 equivalent concentrations, for example, reach 1250, 850, and 600 ppm in A2, A1B, and B1, respectively, by year 2100. Twenty-four modeling centers submitted data from A1B experiments, while 22 submitted data for B1 and 19 provided results from A2 experiments.

Twentieth-century climate model simulations (20C) from 25 CMIP3 GCMs were integrated with historical

TABLE 1. Number of models (N_m) providing output for ψ_{500} , OLR, and $P - E$ fields along with the number of individual realizations (N_r) pooled from all models in a given expt.

| | ψ_{500} | | OLR | | $P - E$ | |
|---------|--------------|-------|-------|-------|---------|-------|
| | N_r | N_m | N_r | N_m | N_r | N_m |
| AMIP2 | 25 | 13 | 26 | 12 | 26 | 12 |
| 20C | 70 | 24 | 70 | 23 | 70 | 22 |
| 20C-A1B | 45 | 23 | 47 | 23 | 43 | 21 |
| B1 | 44 | 21 | 45 | 20 | 44 | 19 |
| A1B | 54 | 23 | 56 | 24 | 52 | 23 |
| A2 | 35 | 17 | 34 | 17 | 39 | 18 |

changes in external forcings such as well mixed greenhouse gases, stratospheric and tropospheric ozone, sulfates, land use, solar irradiance, and volcanic aerosols. All experiments included changes in greenhouse gases and sulfate aerosols, but inclusion of other forcings varied among modeling centers. Many of the 20C experiments terminated in either 1999 or 2000 but the observations extend until at least 2004. For a better comparison with observations, the 20C simulations were extended by appending model simulation data from the start of the SRES A1B scenario to the end of each model's 20C data (20C-A1B). Only 20C runs with branches to A1B runs are used to create 20C-A1B (i.e., the initial conditions for A1B are specified from the end of the corresponding 20C run). For the most direct comparison with observations, 20C-A1B experiments span from 1979 to 2005 for ψ_{500} , and 1979 to 2004 for OLR. Because there are no $P - E$ observations, 20C-A1B $P - E$ trends simply span the 25-yr time period from 1979 to 2003.

Fourteen models from the AMIP2 dataset provide another set of twentieth-century simulations. As with 20C, we consider AMIP2 simulations starting from 1979. The AMIP2 runs terminated before the end of the observational period, with end dates between 1999 and 2003. Because the AMIP2 models are constrained by observed SSTs, it was not possible to extend the simulations further with SRES experiments.

Results from preindustrial control (PIC) simulations were obtained to provide information on internal climate variability in the CMIP3 dataset. We analyze PIC simulations from 24 CMIP3 GCMs yielding over 9000 years of data in total and more than 360 independent estimates of internal climate variability on 25-yr time scales. These estimates allow us to test whether the signals in observations and GCM experiments exceed the level of climate noise.

c. Analysis methods

To investigate Hadley cell widening on decadal time scales, we analyze the model average responses to forcing

TABLE 2. The starting and ending years for each experiment and from each observational dataset. For AMIP2, a range of end years is given since it varies among models.

| | Models | | | | ψ_{500} observations | | | OLR observations | | |
|----------------|-----------|------|---------|-------------|---------------------------|----------|--------|------------------|-------|-------|
| | AMIP2 | 20C | 20C-A1B | B1, A1B, A2 | NCEP-NCAR | NCEP-DOE | ERA-40 | HIRS | ISCCP | GEWEX |
| Starting year | 1979 | 1979 | 1979 | 2000 | 1979 | 1979 | 1979 | 1979 | 1983 | 1983 |
| Ending year(s) | 1999–2003 | 1999 | 2005 | 2099 | 2005 | 2005 | 2001 | 2002 | 2004 | 2004 |

with multimodel ensemble means. We also create multimodel trend distributions by calculating widening in each of the model realizations and pooling the results. These multimodel trend distributions are used to examine the range of widening among various ensembles (or realizations) from all models. Trends in the models are compared with the observed widening in the Hadley cell and with estimates of climate noise from the PIC runs. All trends are given in units of $^{\circ}(\text{lat}) (25 \text{ yr})^{-1}$ unless otherwise specified. Trends from observations, AMIP2, and 20C-A1B experiments since 1979 that span shorter or longer time periods were scaled to 25 yr to approximate the 1979–2003 period for comparison purposes.

Multimodel ensemble mean time series of Hadley cell widths were obtained by first deriving annual-mean Hadley cell widths using ψ_{500} , OLR, and $P - E$ from every realization in each experiment. Ensemble mean time series were obtained for models with more than one realization. PIC and SRES time series were additionally separated into consecutive nonoverlapping 25-yr segments. In these experiments, all time segments from all realizations in a given model were averaged together to obtain an ensemble mean. A multimodel ensemble mean time series was then created by averaging together the individual model ensemble mean time series. The multimodel ensemble mean time series for the AMIP2 experiment spans 1979–99, which is the common time period among these models. Average widening in each experiment was calculated by taking linear trends of these multimodel ensemble means.

Average widening in observational datasets was also examined using ensemble (or multidataset) means. The observations each have slightly different climatological Hadley cell widths and they do not all span identical time periods. To create the ensemble mean, we selected one dataset as a reference and shifted the time series from the other datasets such that their starting widths matched the value of the reference time series at the same date. Such an adjustment has no impact on the trend. It allows us to average all available data together without introducing artificial jumps near the start or end of the time series when there are changes in the number of data points being averaged. Multidataset mean time series are derived separately for OLR and reanalysis datasets.

Multimodel distributions of Hadley cell widening in GCMs were obtained by calculating linear trends from each nonoverlapping time segment in all realizations. Owing to the variability in the modeled years of the AMIP2 experiment, trends were calculated from 1979 until each model's end year (between 1999 and 2003). For the PIC runs, trend distributions consist of about 360 samples each for Hadley cell edges identified by ψ_{500} , OLR, or $P - E$. The actual number of samples depends on how many modeling centers submitted PIC data for the particular variable considered (Table 1). Trend distribution sample sizes for the SRES experiments range from 136 to 208 (e.g., in the A2 scenario there are 34 available realizations from OLR and four 25-yr time segments between 2000 and 2099 yielding 136 trends in the distribution). AMIP2 and 20C-A1B distributions have between 26 and 47 samples.

We present the trends from multimodel ensemble means in favor of mean values from the trend distributions. Although they are similar to one another in most experiments, the distribution means are less representative of the multimodel response. This is because the distribution means may be weighted more by models with a greater number of realizations.

3. Results

Figure 1 shows the annual-mean time series of Hadley cell widths using the ψ_{500} (Fig. 1a) and OLR (Fig. 1b) fields from multimodel ensemble means of PIC and 20C-A1B simulations, along with multidataset ensemble means of observations. Also shown are the 20C-A1B time series from the Geophysical Fluid Dynamics Laboratory (GFDL) Climate Model version 2.0 (CM2.0) model (Table A2) as an example from an individual model. For this figure only, each of the 20C-A1B time series includes A1B simulation data extending until 2099. (The multimodel PIC ensemble mean time series was created by first averaging together consecutive nonoverlapping 120-yr time periods in each of the 24 PIC simulations. These 24 time series were then averaged together to obtain a multimodel ensemble mean.) Widening of the Hadley cell is apparent in observations and 20C-A1B, but it is not until the end of the twenty-first

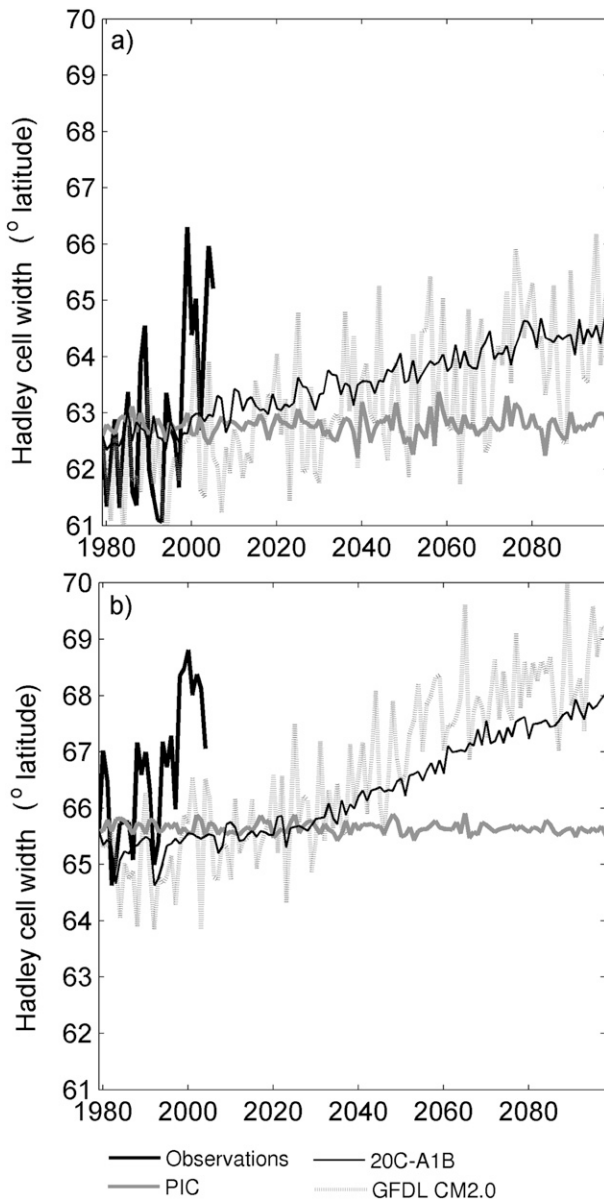


FIG. 1. Time series of annual-mean Hadley cell widths for (a) ψ_{500} and (b) OLR. Thick black lines show the multidataset ensemble mean time series from observations of ψ_{500} and OLR from reanalysis and satellite datasets. Thin black lines show the 20C-A1B time series from multimodel ensemble means of 20C data from 1979 extended until 2099 with A1B data (see section 2b). The 20C-A1B time series from the GFDL CM2.0 model are given by the light gray lines. Dark gray lines give a 120-yr multimodel ensemble mean PIC time series. These 120-yr PIC time series were calculated by averaging consecutive 120-yr time periods together in each model prior to creating a multimodel average. Model time series were shifted so that the starting point of the time series in 1979 matched the width of the observed time series in 1979.

century that Hadley cell widening in 20C-A1B is comparable to observed widening during the past 25 years. Although the projected rate of future widening is smaller than the rate of widening in observations, by 2099 the Hadley cell in 20C-A1B becomes substantially wider than the Hadley cell in the PIC simulations. This is apparent from the multimodel ensemble mean 20C-A1B time series as well as from individual model time series such as the GFDL CM2.0 20C-A1B time series shown in Fig. 1.

There is no tendency in the CMIP3 models without external forcing to shift the Hadley cell toward a wider or narrower state. For example, no discernible trends from either the ψ_{500} or OLR fields are apparent in the PIC time series shown in Fig. 1. Figure 2 shows the multimodel ensemble mean trends [$^{\circ}(\text{lat}) (25 \text{ yr})^{-1}$] from various GCM experiments along with multidataset mean trends from observations, for ψ_{500} (Fig. 2a), OLR (Fig. 2b), and $P - E$ (Fig. 2c) fields. Each trend was derived from a single multimodel ensemble mean time series. Error bars give the 95th percentile confidence interval of the trend with autocorrelation taken into account and reflect interannual variability in the multimodel ensemble mean time series. The averaged observed widening is $3.2^{\circ} \pm 2.1^{\circ}$ and $3.0^{\circ} \pm 1.6^{\circ}$ from ψ_{500} and OLR, respectively. The multimodel ensemble mean trends represent the average response of the models to external forcing (or the lack thereof in the PIC runs). The mean PIC trend is close to zero for each of the three measures of Hadley cell width, which suggests that there is no bias toward Hadley cell widening or narrowing. This is further confirmed in the multimodel trend distributions of PIC calculated from more than 9000 years of simulation time shown in Fig. 3. The PIC trend distributions in Fig. 3 show the range of trends derived from every 25-yr segment in all model ensemble members with no ensemble averaging. PIC trend distributions are zero centered with widening occurring in half the time periods and narrowing in the other half.

On shorter time scales, interannual variability in individual PIC and 20C-A1B ensembles is marginally smaller than the observed variability. Compared to observations, there is much less variability in the multimodel ensemble mean PIC and 20C-A1B time series shown in Fig. 1, but this is largely the result of multimodel averaging. For example, variability in GFDL CM2.0 20C-A1B time series is similar to variability in observations (Fig. 1). Figure 4 shows interannual standard deviations of the annual-mean Hadley cell width from observations and 20C simulations calculated from detrended annual-mean time series of OLR and ψ_{500} from 1979 to 1999. It is clear from Fig. 4 that multimodel ensemble averaging reduces variability in Hadley cell

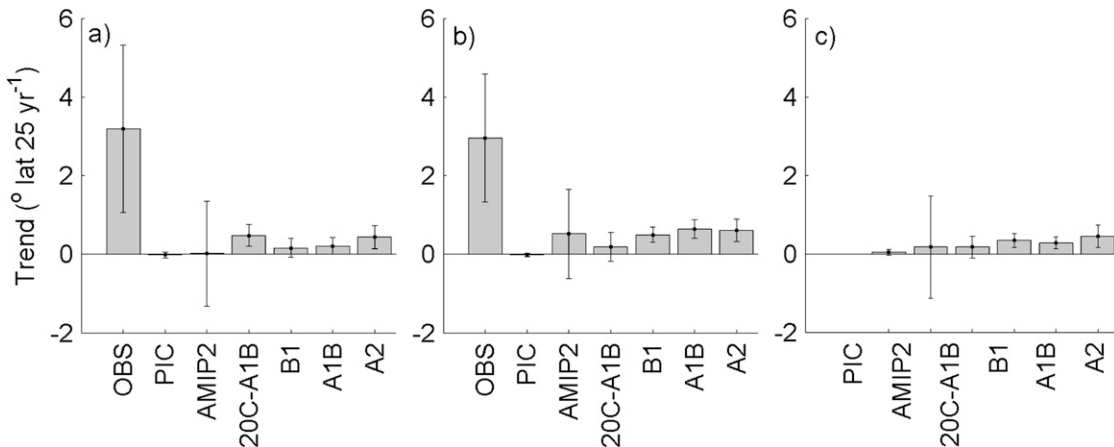


FIG. 2. Trends in Hadley cell width over 25-yr time periods from GCM multimodel ensemble means for (a) ψ_{500} , (b) OLR, and (c) $P - E$. Also shown are observational trends calculated from multidataset means for ψ_{500} (OLR) spanning 1979–2005 (–2004). Error bars give the 95th percentile confidence interval of the trend with autocorrelation taken into account. Each trend from the PIC, B1, A1B, and A2 was calculated from a multimodel ensemble mean time series obtained by averaging together nonoverlapping 25-yr time segments from all models in the experiment (e.g., for the SRES experiments, time series from four consecutive 25-yr time periods in the twenty-first century were averaged together to create a single 25-yr time series in each model; these time series were then combined to create a multimodel average). 20C-A1B trends are from the multimodel ensemble mean covering the same time periods as in OBS. AMIP2 trends are from the multimodel ensemble mean spanning 1979–99 only. All trends are scaled to 25 yr to facilitate comparisons. See section 2c for details on the ensemble averaging.

width since the standard deviations from the multimodel ensemble means are significantly smaller than most of those from individual models. On average, median standard deviations from the models are $\sim 67\%$ – 74% of the median observed values (Fig. 4). It is possible that the models systematically underestimate short-term variability of the Hadley cell, but variability in the observations could also be overestimated as a result of noise in the observing systems. Nonetheless, the similarity between the observed and simulated year-to-year variabilities suggests that the models realistically simulate variations in Hadley cell width on interannual time scales.

Because the simulations of year-to-year variability are realistic and because there is no long-term bias in Hadley cell width in the models, trends in PIC simulations can be considered to be an accurate representation of unforced variability in the climate system. Figure 3 presents multimodel trend distributions derived from each 25-yr time segment from individual ensemble members for every experiment along with the range of trends from the observational datasets. Each box gives the range of trends from the 2.5th to the 97.5th percentile, except for the observation (OBS) boxes which give the entire range of trends from the three individual datasets. The mean of each distribution is represented by a circle and the median is represented by a horizontal bar. Because these distribution means and medians are influenced more by models with a larger number of

ensemble members, they are less representative of the average model response to forcing as given in Fig. 2. In both the ψ_{500} (Fig. 3a) and OLR (Fig. 3b) fields, the lower range of widening from the observations exceeds at least 97.5% of individual PIC ensemble trends. Most of the PIC trends in the distribution fall within $\pm 1.5^\circ$, which is at most only about half of the observed widening. The results from PIC simulations suggest that the observed widening cannot be explained by climate noise.

The observed widening also cannot be explained by changes due to external forcings. Mean widening in the observations is significantly larger than widening in the 20C-A1B and SRES experiments. The largest trends in the GCM simulations are $\sim 0.6^\circ$ from the OLR fields in A1B and A2, which is only $\sim 1/5$ of the observed widening (Fig. 2b). At least 97.5% of ψ_{500} and OLR based trends from individual realizations in the 20C-A1B and SRES experiments are also smaller than the observations (Figs. 3a,b). The distributions of trends from $P - E$, which show close agreement to the OLR distributions, are also smaller than widening in the observational datasets (Fig. 3c). In addition to being smaller than the widening in the observations, most of the widening in the GCMs falls within the range of climate noise, as evidenced by the sizable overlap between distributions of trends between the PIC and other GCM experiments in Fig. 3.

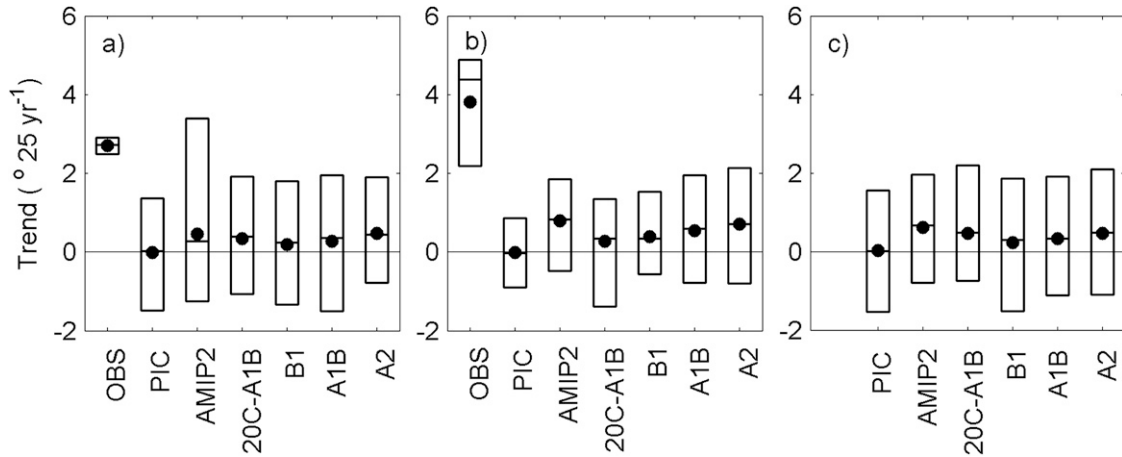


FIG. 3. Distributions of trends in the Hadley cell width from individual datasets for the observations and from all realizations in the GCMs. Trends are shown for widening identified by (a) ψ_{500} , (b) OLR, and (c) $P - E$. Each box gives the range of trends from the 2.5th to the 97.5th percentile, except for the observation (OBS) boxes, which give the entire range of trends from the three individual datasets. The mean of each distribution is represented by a circle and the median is represented by a horizontal bar.

Even though widening in the GCM simulations is weak relative to observations, positive mean trends are found in all experiments in both the twentieth and twenty-first centuries (see Fig. 2), although the mean ψ_{500} trend in AMIP2 is very small. Additionally, median trends from the pool of all available realizations show that widening is more common than narrowing in these experiments (Fig. 3). For example, widening is found in 17 of the 25 realizations based on ψ_{500} , and in 25 (19) of the 26 realizations based on OLR ($P - E$). The simulated widening indicates that the Hadley cell is re-

sponding to one or more forcings in the models. Furthermore, the mean values from each distribution of trends in the SRES experiments are significant at a level exceeding 99.9% using the Student's t test (Fig. 3). Multimodel ensemble mean widening from the OLR and $P - E$ fields in all SRES experiments and from the SRES A2 ψ_{500} field are also significant (Fig. 2).

It is not clear from the GCMs whether widening projected during this century will be larger or smaller than that of the twentieth century. The mean 20C-A1B trend from ψ_{500} of $0.48^\circ \pm 0.3^\circ$ is larger than all the

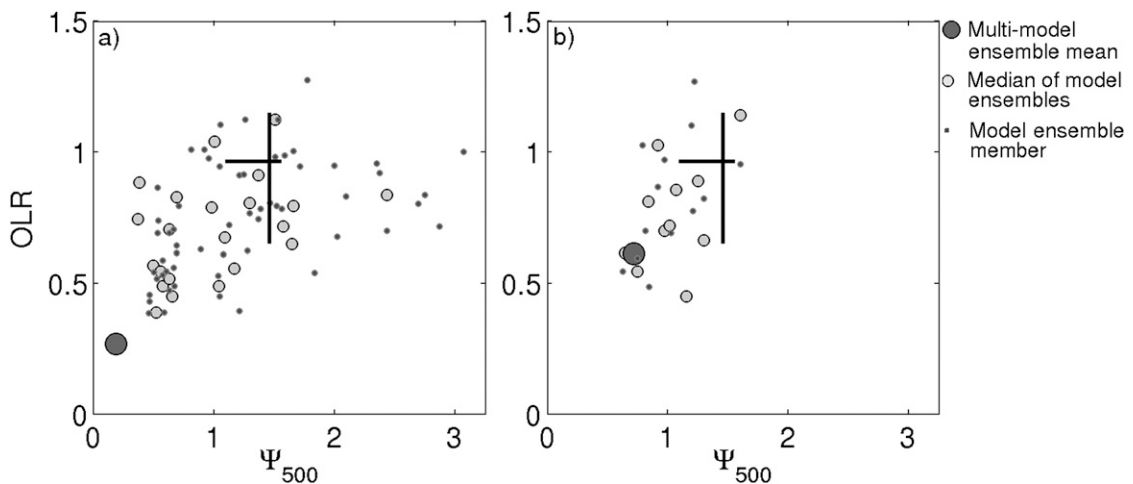


FIG. 4. Interannual standard deviations of the annual-mean Hadley cell width from 1979 to 1999 from observations (crossbars), multimodel ensemble means (large circles), and individual model ensemble members (small circles) for the (a) 20C and (b) AMIP2 experiments. The medians of model ensembles are given by the medium size circles. All time series were detrended prior to calculating the standard deviations. The observed standard deviations are centered at the median value among datasets. Only models providing output for both ψ_{500} and OLR are included here.

SRES ψ_{500} trends (Fig. 2a). On the other hand, the 20C-A1B trends from OLR and $P - E$ of $0.19^\circ \pm 0.4^\circ$ and $0.18^\circ \pm 0.3^\circ$, respectively, are smaller than the widening in the SRES experiments (Figs. 2b,c). The only significant trend in the 20C-A1B runs is from the ψ_{500} field.

The AMIP2 experiments, which are forced with observed SSTs, do not show more widening than 20C-A1B simulations. The average AMIP2 trends of $0.02^\circ \pm 1.3^\circ$, $0.5^\circ \pm 1.1^\circ$, and $0.18^\circ \pm 1.3^\circ$ from multimodel ensemble mean time series of ψ_{500} , OLR, and $P - E$, respectively, have the greatest uncertainties among all experiments (Fig. 2). Large uncertainty in these trends is due in part to the shorter time span of the multimodel mean ending in 1999, but it is also related to the interannual variability in the AMIP2 simulations (Fig. 4b). Although a significant part of the observed widening occurs after 2000 (see Fig. 1), the shorter time period in the AMIP2 simulations does not account for the weaker widening in these models relative to observations. Multidataset mean widening of 1.6° and $2.0^\circ (21 \text{ yr})^{-1}$ from ψ_{500} and OLR, respectively, in the observational datasets from 1979 to 1999 is larger than the multimodel mean AMIP2 trends over the same time period by at least a factor of 4. The Beijing Climate Center (BCC) model (Table A2) has two out of four realizations in AMIP2 with trends from ψ_{500} exceeding the observed value of 3° ; these trends account for the upper limit of the ψ_{500} range in Fig. 3a. The BCC model was the only one of the AMIP2 simulations forced with SSTs extending until 2003. Most of the widening occurred after 2000 in one of the BCC realizations but before 2000 in the other. Thus, the larger trends in this model are not necessarily the result of extending the AMIP2 experiment until 2003.

A comparison of widening from 1979 to 1999 between observations and GCM simulations of the twentieth century is shown in Fig. 5. Widening from each model realization is given by the small circles for the 20C simulations (Fig. 5a) and AMIP2 simulations (Fig. 5b) from models that provide data for both OLR and ψ_{500} . Ensemble mean widening from each of the models is given by the medium circles, and the multimodel ensemble mean widening among all models is given by the large circle. The ranges of observed widening are given by the crossbars, which are centered at the multidataset mean widening of 1.6° and $2.0^\circ (21 \text{ yr})^{-1}$ from the ψ_{500} and OLR datasets. Data from the BCC AMIP2 model, which includes realizations with trends comparable to observations, was not included in this figure since it did not provide OLR output. From 1979 to 1999 multimodel ensemble mean widening, as well as trends in each of the model ensemble means, is smaller than the ranges of observed widening in the 20C and AMIP2 simulations. Given that the relatively smaller observed widening

from 1979 to 1999 is not captured in the AMIP2 model simulations over this time period (Fig. 5b), it is unlikely that the sustained widening that occurred after the year 2000 would be reproduced in the AMIP2 simulations if they were extended until 2005. In the 20C simulations, widening based on ψ_{500} from 13 of the 65 realizations in the models that provide output for both OLR and ψ_{500} is within the range of the observed widening from ψ_{500} , but none of the realizations show widening comparable to the OLR observational datasets (Fig. 5a). Even though much of the observed widening occurred after the year 2000, the widening that occurred prior to 2000 still is not captured in the majority of the GCM simulations of the twentieth century.

There is a general tendency for the edges of the subtropical dry zone identified by $P - E$ and OLR to shift farther poleward than the Hadley cell edges given by ψ_{500} , in agreement with Lu et al. (2007). This is apparent in the mean SRES trends (Fig. 2) and in the distributions of widening from both $P - E$ and OLR in the SRES experiments, which are shifted toward higher values relative to the ψ_{500} distributions (Fig. 3). Such enhanced displacements are also found in AMIP2; multimodel mean widening from OLR and $P - E$ is larger than widening from ψ_{500} , and trend distributions of the former also indicate a tendency for greater widening. Additionally, widening in two of the three OLR observations exceed the three ψ_{500} trends from reanalysis. It is only in 20C-A1B that widening from ψ_{500} exceeds that of OLR and $P - E$. In 20C-A1B simulations, the average trend from ψ_{500} is more than twice as large as the OLR and $P - E$ trends. However, almost all observational and model evidence suggests that the edges of the subtropical dry zone identified by $P - E$ and OLR might have a larger displacement.

4. Mechanisms for widening

There are four plausible mechanisms that may be responsible for the widening of the tropical belt. Here we will discuss these mechanisms in the context of observed and simulated Hadley cell widening.

a. Stratospheric cooling

Changes in stratospheric circulation have been shown to influence tropospheric climate in models and observations. Idealized GCM simulations show that polar stratospheric cooling and the accompanying increase in stratospheric winds are associated with a stronger, more poleward subtropical tropospheric jet (Polvani and Kushner 2002). Conversely, a more equatorward jet is found to be associated with observed polar stratospheric warming during times of solar maxima in the NCEP-NCAR reanalysis (Haigh et al. 2005).

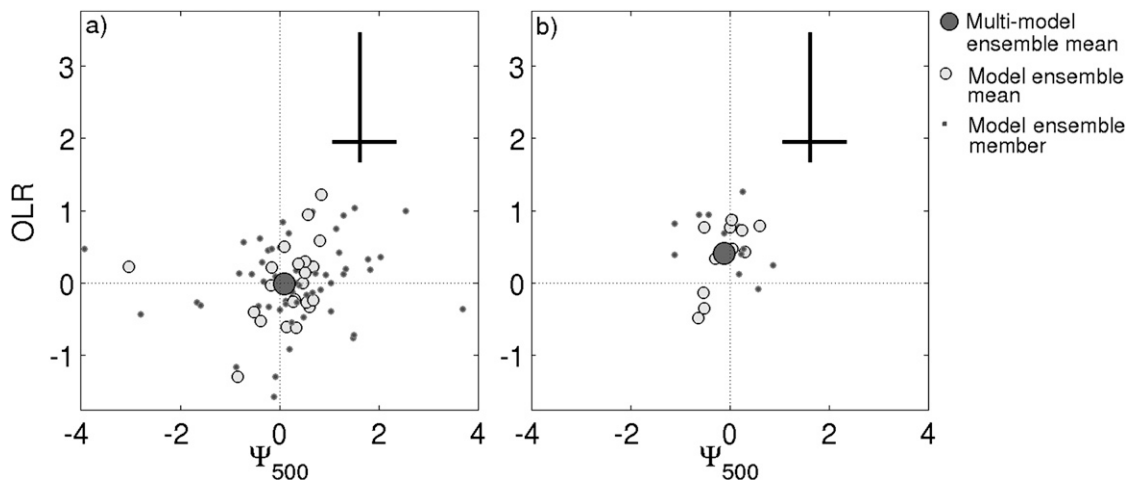


FIG. 5. Widening of the Hadley cell from 1979 to 1999 [$^{\circ}(\text{lat}) (21 \text{ yr})^{-1}$] from ψ_{500} and OLR in observations and (a) GCM simulations of 20C and (b) AMIP2. The range of observed widening from individual datasets is given by the crossbars, which are centered at the multidataset mean widening. Also shown is the multimodel ensemble mean widening (large circles), ensemble mean widening from each individual model (medium circles), and widening from each model ensemble member (small circles). Only models providing output for both ψ_{500} and OLR are included here.

In recent decades, ozone depletion as well as the increase of greenhouse gases have lead to strong cooling of the Antarctic polar stratosphere, resulting in an increase in the Southern Hemisphere annular mode (SAM) index toward positive polarities (Thompson and Solomon 2002; Gillett and Thompson 2003). The strengthening of the SAM is reproduced in CMIP3 simulations of twentieth-century climate since 1950, with trends from models including stratospheric ozone depletion in close agreement with the observed trend (Cai and Cowan 2007). Previdi and Liepert (2007) show that the positive trend in the SAM index from A2 simulations accounts for about half of the displacement of the Hadley cell edges in the Southern Hemisphere over the next 100 years. We would therefore expect the subset of 20C models that includes stratospheric ozone depletion to show larger widening than those without it. From 1979 to 1999, multimodel ensemble mean widening trends in the subset of 20C models that include ozone depletion are 0.035° , -0.022° , and $-0.082^{\circ} (21 \text{ yr})^{-1}$ from ψ_{500} , OLR, and $P - E$, respectively. However, larger trends are found from the subset of models that do not include ozone depletion, which are 0.27° , 0.035° , and $0.15^{\circ} (21 \text{ yr})^{-1}$ from ψ_{500} , OLR, and $P - E$, respectively. The models without ozone depletion show between 0.057° and 0.24° more widening over this time period than those that include ozone depletion.

Strong stratospheric cooling since 1979 and the strengthening of the polar stratospheric vortex during the austral spring (Thompson and Solomon 2002) may explain some of the displacement of the Southern Hemisphere Hadley cell edges in the spring season. The

20C multimodel ensemble mean time series from ψ_{500} , OLR, and $P - E$ all show poleward displacements of the spring season Southern Hemisphere Hadley cell edge from 1979 to 1999. In the models that include ozone depletion, the Southern Hemisphere Hadley cell edge displacement trends are 0.23° , 0.053° , and $0.15^{\circ} (21 \text{ yr})^{-1}$ for ψ_{500} , OLR, and $P - E$, respectively. Similar, but slightly smaller, trends are found in the multimodel ensemble mean time series from models that do not include ozone depletion: 0.22° , 0.031° , and $0.087^{\circ} (21 \text{ yr})^{-1}$ for ψ_{500} , OLR, and $P - E$, respectively. While ozone depletion in the models may have contributed to Hadley cell widening, the similarities between trends in models with and without ozone depletion imply that it is not solely responsible for the poleward displacement of the Southern Hemisphere Hadley cell branch.

In general, CMIP3 models are not designed to simulate the effects of the stratosphere on climate change (Baldwin et al. 2007). The weak response of the annular modes to volcanic forcing in CMIP3 GCM simulations of the twentieth century suggests that these models may be underestimating stratosphere–troposphere coupling (Miller et al. 2006). If so, it may explain at least part of the discrepancy between the observed Hadley cell widening and the relatively feeble trends in the twentieth-century simulations. Despite the limited representation of the stratosphere in the CMIP3 simulations, there is no indication that model vertical resolutions affect the Hadley cell widening. Correlations between widening and the number of vertical levels are at most 0.26 among the three variables from the 20C-A1B experiments. Thus, the vertical resolution explains less than 7% of the

trend variance among the 20C-A1B models. Horizontal resolution explained a similarly small fraction of the variance in widening among the models. A larger correlation of 0.4 was found between 20C-A1B trends and model top heights from the OLR field, but it is likely spurious since correlations from the ψ_{500} and $P - E$ fields were only ~ 0.2 .

b. Global warming

Held (2000) postulated that the extent of the Hadley cell is determined by the latitude of baroclinic instability. An increase in static stability suppresses baroclinic growth rates such that the onset of baroclinicity is shifted poleward and the cell widens. This relationship is supported by GCM studies in which midlatitude static stability (or a close proxy) increases with the Hadley cell width as suggested by Held (2000; Lu et al. 2007; Frierson et al. 2007).

Idealized and comprehensive GCMs show that increases in Hadley cell width are related to higher global mean temperatures by an increase in midlatitude static stability (Lu et al. 2007; Frierson et al. 2007). CMIP3 GCMs show dry static stability increasing throughout the midlatitudes in accordance with the moist adiabat in the A1B scenario (Frierson 2006). As SSTs warm, additional moisture is introduced into the troposphere, increasing static stability and the poleward extent of the Hadley cell. Using ψ_{500} as an indicator of Hadley cell edges, idealized GCMs and A2 simulations from the CMIP3 archive found an increase in the Hadley cell width of $0.4\text{--}0.6\text{ K}^{-1}$ global warming (Lu et al. 2007; Frierson et al. 2007). Average surface warming in the CMIP3 dataset is $0.16\text{ K decade}^{-1}$ from 1979 to 1999 (Karl et al. 2006). Over the same time period, the Hadley cell identified by ψ_{500} widens by $0.14\text{ K decade}^{-1}$ in 20C-A1B. Thus, the rate of widening in the model simulations of the twentieth century is $\sim 0.87\text{ K}^{-1}$. The enhanced rate of widening in the historical simulations suggests that global warming in the models may not be the only factor causing the widening of the Hadley cell in the past few decades. But, all of the above GCM estimates are an order of magnitude smaller than the observed rate of $\sim 6\text{ K}^{-1}$ (Hu and Fu 2007).

c. Pacific and Indian Ocean warming

The pattern of surface warming may also contribute to Hadley cell widening. The observed SSTs explain a substantial fraction of the interannual Hadley cell variability in the AMIP2 models: correlations between the multimodel ensemble mean time series and the multidataset mean time series are 0.57 and 0.80 from ψ_{500} and OLR, respectively. Additionally, atmospheric GCMs forced with observed SSTs show that anomalous

warmth in the Indo-western Pacific is sufficient to shift the zonal mean circulation poleward (Lau et al. 2008). Consequently, warming in the west Pacific over the past few decades may be responsible for the poleward displacement of the subtropical jets (Fu et al. 2006). If surface warming during the past few decades were the primary influence on Hadley cell broadening, then significant widening should be seen in the AMIP2 simulations. This is because the surface warming in these experiments matches the observed warming. Widening in AMIP2 is smaller than observations with only 2 out of 57 realizations having trends from ψ_{500} or OLR comparable to observations. If the AMIP2 model responses are reliable, then global warming during the past few decades could not have been the cause of the widening.

d. Changes in baroclinic-eddy phase speeds

An alternate mechanism to explain the recent widening suggested by Chen and Held (2007) relies on upper-tropospheric warming and polar stratospheric cooling (either together or individually) to increase zonal wind shear across the tropopause. They propose that the increase in the zonal mean winds increases the phase speeds of baroclinic eddies and causes a poleward shift in the tropospheric circulation. This mechanism was identified both in GCMs and observations, although the GCM response was weaker than the observations (Chen and Held 2007).

5. Conclusions

Given that idealized and comprehensive GCMs have shown Hadley cell widening in response to increases in greenhouse gases and changes in the thermal structure of the polar stratosphere (Lu et al. 2007; Frierson et al. 2007; Polvani and Kushner 2002), it is likely that the observed widening is due to global warming and stratospheric ozone depletion. Simultaneous global warming and stratospheric cooling may have also acted together to increase the phase speed of the baroclinic eddies and widen the Hadley cell (Chen and Held 2007). However, widening in GCM simulations of the twentieth century is significantly smaller than observations, even in the models that include both greenhouse gas forcing and stratospheric ozone depletion.

If natural variation in Hadley cell width of less than 1.5° as given by the CMIP3 control simulations is a realistic estimate, we can assume that the observed widening of the Hadley cell by $\sim 3^\circ$ in the last 25 years is significant. It is also possible that the model responses to forcing are too small. GCMs do show widening on average in the twentieth century, but it is weak compared

to observations. Alternatively, there may be unidentified mechanisms in the models working in the opposite direction that counteract the widening related to ozone depletion and greenhouse gas warming.

We have demonstrated that the GCMs in the CMIP3 multimodel dataset are unable to reproduce the recent Hadley cell widening but additional work must be completed so as to understand why widening in the GCMs is so much smaller than observed. Widespread agreement among six disparate sets of observations suggests that the recent Hadley cell widening is real and not the result of artifacts in the observing systems (Seidel et al. 2008). Because the poleward boundaries of the Hadley cell are associated with the desert regions of the world, it is important to simulate changes to these boundaries and accurately predict how they may change in response to external forcings in the future.

The past 25 years is an optimal time period to test GCM simulations of the Hadley cell. The availability of multiple observations of Hadley cell widening allows direct comparisons between model simulations and observations. More importantly, the past few decades are special because they span a period of simultaneous global warming and stratospheric ozone depletion, both of which may contribute to observed widening. The failure of GCMs to simulate widening over this

time period highlights the need for better understanding of the Hadley cell and improvements in GCM simulations.

Acknowledgments. We thank D. Frierson and J. M. Wallace for useful discussions and helpful comments on this manuscript. We acknowledge the modeling groups, the Program for Climate Model Diagnosis and Intercomparison (PCMDI), and the WCRP Working Group on Coupled Modeling (WGCM) for their roles in making available the WCRP CMIP3 multimodel dataset. Support of this dataset is provided by the Office of Science, U.S. Department of Energy. This study is supported by NOAA Grant NA08OAR4310725.

APPENDIX

Technical Details of Models

Tables A1 and A2 show details of the models used in this study. Table A1 lists the models providing ψ_{500} , OLR, and $P - E$ data for each experiment. The CMIP3 model horizontal resolutions, model tops, and number of vertical layers are given in Table A2. These values were obtained from each model's atmospheric component.

TABLE A1. Model outputs available from each experiment. An "X" denotes models in which ψ_{500} , OLR, and $P - E$ data are all available for a given scenario. "M," "O," and "P" denote models providing data for only ψ_{500} , OLR, or $P - E$, respectively.

| Expt | 20C | 20C-A1B | AMIP2 | A2 | A1B | B1 | PIC |
|-----------------|-----|---------|-------|----|-----|----|-----|
| BCC-CM1 | M | - | M | - | - | M | - |
| BCCR-BCM2.0 | X | X | - | X | X | X | X |
| CGCM3.1(T47) | X | X | - | X | X | X | X |
| CGCM3.1(T63) | X | X | - | - | X | X | X |
| CNRM-CM3 | X | MO | X | X | MO | X | X |
| CSIRO-MK3.0 | X | X | - | X | X | X | X |
| CSIRO-MK3.5 | MP | MP | - | MP | X | X | X |
| GFDL-CM2.0 | X | X | - | X | X | X | X |
| GFDL-CM2.1 | MO | MO | MO | MO | X | MO | MO |
| GISS-AOM | X | X | - | - | X | X | X |
| GISS-EH | X | X | - | - | X | - | X |
| GISS-ER | X | X | X | X | X | X | X |
| IAP FGOALS-g1.0 | X | X | X | - | X | X | X |
| INGV-ECHAM-4 | X | X | - | P | X | - | X |
| INM-CM3.0 | X | X | X | X | X | X | X |
| IPSL-CM4 | X | X | OP | X | X | X | X |
| MIROC3.2(H) | X | X | X | - | X | X | X |
| MIROC3.2(M) | MO | MO | X | X | X | X | X |
| MIUB ECHO-G | OP | OP | - | OP | OP | OP | OP |
| MPI ECHAM5 | X | X | X | X | X | X | X |
| MRI-CGCM2.3.2 | X | - | X | X | X | X | X |
| NCAR CCSM3 | X | X | X | X | X | X | X |
| NCAR PCM | X | - | MP | X | X | M | X |
| UKMO-HadCM3 | X | X | - | X | X | X | X |
| UKMO-HadGEM1 | X | X | X | X | X | - | X |

TABLE A2. Resolution for the atmospheric component of the CMIP3 models. Horizontal resolution is given for spectral and grid point models in terms of triangular truncation or lat–lon grid spacing. N_L refers to the number of vertical levels. The model top is also given for each model in units of hPa except where otherwise noted. A “?” denotes insufficient model documentation.

| Expt | Resolution | N_L | Model top (hPa) |
|-----------------|---------------------------------|-------|-----------------|
| BCC-CM1 | T63 | 16 | 25 |
| BCCR-BCM2.0 | T63 | 31 | 10 |
| CGCM3.1(T47) | T47 | 31 | 1 |
| CGCM3.1(T63) | T63 | 31 | 1 |
| CNRM-CM3 | T63 | 45 | 0.05 |
| CSIRO-MK3.0 | T63 | 18 | 4.5 |
| CSIRO-MK3.5 | T63 | 18 | 4.5 |
| GFDL-CM2.0 | $2.0^\circ \times 2.5^\circ$ | 24 | 3 |
| GFDL-CM2.1 | $2.0^\circ \times 2.5^\circ$ | 24 | 3 |
| GISS-AOM | $3.0^\circ \times 4.0^\circ$ | 12 | 10 |
| GISS-EH | $4.0^\circ \times 5.0^\circ$ | 20 | 0.1 |
| GISS-ER | $4.0^\circ \times 5.0^\circ$ | 20 | 0.1 |
| IAP FGOALS-g1.0 | T42 | 26 | 2.2 |
| INGV-ECHAM-4 | T106 | 19 | 10 |
| INM-CM3.0 | $4.0^\circ \times 5.0^\circ$ | 21 | 10 |
| IPSL-CM4 | $2.5^\circ \times 3.75^\circ$ | 19 | ? |
| MIROC3.2(H) | T106 | 56 | 40 km |
| MIROC3.2(M) | T42 | 20 | 30 km |
| MIUB ECHO-G | T30 | 19 | 10 |
| MPI ECHAM5 | T63 | 19 | 10 |
| MRI-CGCM2.3.2 | T42 | 30 | 0.4 |
| NCAR CCSM3 | T85 | 26 | 2.2 |
| NCAR PCM | T42 | 26 | 2.2 |
| UKMO-HadCM3 | $2.75^\circ \times 3.75^\circ$ | 19 | 10 |
| UKMO-HadGEM1 | $1.25^\circ \times 1.875^\circ$ | 38 | 3.1 |

REFERENCES

- Baldwin, M. P., M. Dameris, and T. G. Shepherd, 2007: How will the stratosphere affect climate change? *Science*, **316**, 1576–1577.
- Cai, W. J., and T. Cowan, 2007: Trends in Southern Hemisphere circulation in IPCC AR4 models over 1950–99: Ozone depletion versus greenhouse forcing. *J. Climate*, **20**, 681–693.
- Chen, G., and I. M. Held, 2007: Phase speed spectra and the recent poleward shift of Southern Hemisphere surface westerlies. *Geophys. Res. Lett.*, **34**, L21805, doi:10.1029/2007GL031200.
- Eyring, V., and Coauthors, 2007: Multimodel projections of stratospheric ozone in the 21st century. *J. Geophys. Res.*, **112**, D16303, doi:10.1029/2006JD008332.
- Frierson, D. M. W., 2006: Robust increases in midlatitude static stability in simulations of global warming. *Geophys. Res. Lett.*, **33**, L24816, doi:10.1029/2006GL027504.
- , J. Lu, and G. Chen, 2007: Width of the Hadley cell in simple and comprehensive general circulation models. *Geophys. Res. Lett.*, **34**, L18804, doi:10.1029/2007GL031115.
- Fu, Q., C. M. Johanson, J. M. Wallace, and T. Reichler, 2006: Enhanced mid-latitude tropospheric warming in satellite measurements. *Science*, **312**, 1179.
- Gates, W. L., and Coauthors, 1999: An overview of the results of the Atmospheric Model Intercomparison Project (AMIP I). *Bull. Amer. Meteor. Soc.*, **80**, 29–55.
- Gillett, N. P., and D. W. J. Thompson, 2003: Simulation of recent Southern Hemisphere climate change. *Science*, **302**, 273–275.
- Haigh, J. D., M. Blackburn, and R. Day, 2005: The response of tropospheric circulation to perturbations in lower-stratospheric temperature. *J. Climate*, **18**, 3672–3685.
- Held, I. M., 2000: The general circulation of the atmosphere. *Geophysical Fluid Dynamics Program*, Woods Hole Oceanographic Institute, 70 pp.
- Hu, Y., and Q. Fu, 2007: Observed poleward expansion of the Hadley circulation since 1979. *Atmos. Chem. Phys.*, **7**, 5229–5236.
- Hudson, R. D., A. D. Frolov, M. F. Andrade, and M. B. Follette, 2003: The total ozone field separated into meteorological regimes. Part I: Defining the regimes. *J. Atmos. Sci.*, **60**, 1669–1677.
- , M. F. Andrade, M. B. Follette, and A. D. Frolov, 2006: The total ozone field separated into meteorological regimes—Part II: Northern Hemisphere mid-latitude total ozone trends. *Atmos. Chem. Phys.*, **6**, 5183–5191.
- Kanamitsu, M., and Coauthors, 2002: NCEP dynamical seasonal forecast system 2000. *Bull. Amer. Meteor. Soc.*, **83**, 1019–1037.
- Karl, T. R., S. J. Hassol, C. D. Miller, and W. L. Murray, Eds., 2006: Temperature trends in the lower atmosphere: Steps for understanding and reconciling differences. U.S. Climate Change Science Program Synthesis and Assessment Product 1.1, 180 pp.
- Kistler, R., and Coauthors, 2001: The NCEP–NCAR 50-Year Reanalysis: Monthly means CD-ROM and documentation. *Bull. Amer. Meteor. Soc.*, **82**, 247–267.
- Lau, N. C., A. Leetmaa, and M. J. Nath, 2008: Interactions between the responses of North American climate to El Niño–La Niña and to the secular warming trend in the Indian–Western Pacific oceans. *J. Climate*, **21**, 476–494.
- Lu, J., G. A. Vecchi, and T. Reichler, 2007: Expansion of the Hadley cell under global warming. *Geophys. Res. Lett.*, **34**, L06805, doi:10.1029/2006GL028443.
- Meehl, G. A., C. Covey, T. Delworth, M. Latif, B. McAvaney, J. F. B. Mitchell, R. J. Stouffer, and K. E. Taylor, 2007: The WCRP CMIP3 multimodel dataset: A new era in climate change research. *Bull. Amer. Meteor. Soc.*, **88**, 1383–1394.
- Mehta, A., and J. Susskind, 1999: Outgoing longwave radiation from the TOVS Pathfinder Path A data set. *J. Geophys. Res.*, **104**, 12 193–12 212.
- Miller, R. L., G. A. Schmidt, and D. T. Shindell, 2006: Forced annual variations in the 20th century Intergovernmental Panel on Climate Change Fourth Assessment Report models. *J. Geophys. Res.*, **111**, D18101, doi:10.1029/2005JD006323.
- Nakicenovic, N., and R. Swart, Eds., 2000: *Special Report on Emissions Scenarios*. Cambridge University Press, 570 pp.
- Polvani, L. M., and P. J. Kushner, 2002: Tropospheric response to stratospheric perturbations in a relatively simple general circulation model. *Geophys. Res. Lett.*, **29**, 1114, doi:10.1029/2001GL014284.
- Previdi, M., and B. G. Liepert, 2007: Annular modes and Hadley cell expansion under global warming. *Geophys. Res. Lett.*, **34**, L22701, doi:10.1029/2007GL031243.
- Seidel, D. J., and W. J. Randel, 2007: Recent widening of the tropical belt: Evidence from tropopause observations. *J. Geophys. Res.*, **112**, D20113, doi:10.1029/2007JD008861.
- , Q. Fu, W. J. Randel, and T. J. Reichler, 2008: Widening of the tropical belt in a changing climate. *Nat. Geosci.*, **1**, 21–24.
- Solomon, S., D. Qin, M. Manning, M. Marquis, K. Averyt, M. M. B. Tignor, H. L. Miller Jr., and Z. Chen, Eds., 2007: *Climate Change 2007: The Physical Science Basis*. Cambridge University Press, 996 pp.
- Stackhouse, P. W., Jr., S. K. Gupta, S. J. Cox, J. C. Mikovitz, T. Zhang, and M. Chiacchio, 2004: 12-year surface radiation

- budget data set. *GEWEX News*, Vol. 14, No. 4, International GEWEX Project Office, Silver Spring, MD, 10–12.
- Thompson, D. W. J., and S. Solomon, 2002: Interpretation of recent Southern Hemisphere climate change. *Science*, **296**, 895–899.
- Uppala, S. M., and Coauthors, 2005: The ERA-40 Re-Analysis. *Quart. J. Roy. Meteor. Soc.*, **131**, 2961–3012.
- Wallace, J. M., and P. V. Hobbs, 2006: *Atmospheric Science: An Introductory Survey*. 2nd ed. Academic Press, 483 pp.
- Yin, J. H., 2005: A consistent poleward shift of the storm tracks in simulations of 21st century climate. *Geophys. Res. Lett.*, **32**, L18701, doi:10.1029/2005GL023684.
- Zhang, Y., W. B. Rossow, A. A. Lacis, V. Oinas, and M. I. Mishchenko, 2004: Calculation of radiative fluxes from the surface to top of atmosphere based on ISCCP and other global data sets: Refinements of the radiative transfer model and the input data. *J. Geophys. Res.*, **109**, D19105, doi:10.1029/2003JD004457.